CrossMark

ORIGINAL ARTICLE

Effect of viscosity and wall heat conduction on shock attenuation in narrow channels

A. Deshpande · B. Puranik

Abstract   In the present work, the effects due to viscosity and wall heat conduction on shock propagation and attenuation in narrow channels are numerically investigated. A two-dimensional viscous shock tube configuration is simulated, and heat conduction in the channel walls is explicitly included. The simulation results indicate that the shock attenuation is significantly less in the case of an adiabatic wall, and the use of an isothermal wall model is adequate to take into account the wall heat conduction. A parametric study is performed to characterize the effects of viscous forces and wall heat conduction on shock attenuation, and the behaviour is explained on the basis of boundary layer formation in the post-shock region. A dimensionless parameter that describes the shock attenuation is correlated with the diaphragm pressure ratio and a dimensionless parameter which is expressed using the characteristic Reynolds number and the dimensionless shock travel.

Keywords   Shock attenuation · Viscous dissipation · Conjugate heat transfer · Viscous shock tube

1 Introduction

Shock wave motion in large shock tubes at relatively high Reynolds numbers is well approximated by the ideal shock tube theory. Recent medical and industrial applications of shock waves necessitate a better understanding of shock wave motion at low Reynolds numbers (e.g., shock waves at micro-scales), where the effects of friction and heat transfer at the walls are expected to be significant. Recently, the use of shock waves at micro-scales has been envisioned in several MEMS applications. Such applications require a deeper insight into the mechanisms governing the behaviour of shock waves at micro-scales, where the shock wave motion is governed by viscosity as well as convection. Shock and compression waves propagating in small channels are also highly relevant to reactive flow situations such as combustion or detonation phenomena in micro-channels.

In the past, analogous situations have been analysed. In particular, Duff [1], Roshko [2] and Mirels [3,4] investigated several physical aspects of conventional shock tubes operating at low initial pressures, and showed that such shock tubes do not perform as predicted by the ideal shock tube theory. The propagation of shock waves in narrow channels has been studied experimentally and numerically by Sun et al. [5]. Brouillette [6], Mirshekari and Brouillette [7], and Ngomo et al. [8] have developed one-dimensional models to account for the effect of scale on the propagation of shock waves. The effects of friction and heat transfer were also incorporated in these models. The propagation and attenuation of shock waves in microchannels have been studied numerically, both using the Navier–Stokes equations with or without slip at the wall, and using particle-based simulation techniques such as the Direct Simulation Monte Carlo method (for example, Zeitoun and Burtschell [9], Zeitoun et al. [10], Parisse et al. [11], Shoev et al. [12,13], Austin and Bodony [14], Arun and Kim [15]). Recently, Mirshekari et al. [16] fabricated and tested a fully instrumented micro-scale shock tube to study the transmission of a shock wave, produced in a large (37 mm) shock tube, into

A. Deshpande · B. Puranik (✉)
Department of Mechanical Engineering,
Indian Institute of Technology Bombay, Mumbai, India
e-mail: puranik@iitb.ac.in

A. Deshpande
e-mail: arvind_deshpande@iitb.ac.in

a 34 μm hydraulic diameter and 2 mm long microchannel. The experimental results were compared with various analytical and numerical models, and the best agreement was obtained with two-dimensional Navier–Stokes fluid dynamics computation, which assumes a no-slip, isothermal wall boundary condition. Good agreement was also obtained with a simple shock tube laminar boundary layer model. It was observed that shock wave propagation in a microchannel exhibits behaviour similar to that observed in large-scale facilities operated at low pressures, and the shock attenuation can be explained in terms of accepted laminar boundary layer models.

We observe that the one-dimensional models indirectly incorporated viscous and heat conduction effects, while the two-dimensional simulations focused on investigating the effect of viscous forces. The effect of heat conduction in the walls confining the flow channel was considered indirectly using different boundary conditions such as adiabatic and isothermal walls. Mirshekari and Brouillette [7] suggested that a microscale shock tube should be made out of materials with lower thermal conductivity such as quartz or Pyrex to decrease the thermal dissipation rate. Parisse et al. [11] suggested simulation of wall heat transfer along with fluid flow for precise description of the heat exchange between the solid wall and the fluid. It may be noted that wall heat conduction is an independent effect influencing shock attenuation, the physical mechanism being heat loss from the post-shock region. The ideal inviscid theory assumes adiabatic boundaries (zero heat loss from the post-shock region), thus resulting in no shock attenuation.

In view of the foregoing observations, the objective of the present work is to characterize the effect of viscous forces as well as that of wall heat conduction on shock propagation and attenuation in narrow channels. We employ two-dimensional Navier–Stokes equations, along with conjugate heat transfer at the channel wall-fluid interface. Thus, the heat conduction through the material of the shock tube wall is explicitly incorporated, and its effect on the shock propagation and attenuation is studied.

2 Governing equations and benchmarking of the solver

The viscous compressible form of the Navier–Stokes equations is employed for the simulations of the shock channel (the usage shock "channel" is to convey that our geometry is planar two-dimensional and not axi-symmetric) flow, along with the energy equation that includes the viscous dissipation. These are given by

$$\frac{\partial U}{\partial t} + \frac{\partial F}{\partial x} + \frac{\partial G}{\partial y} = 0 \qquad (1)$$

where the vectors U, F and G are given by

$$U = \begin{bmatrix} \rho \\ \rho u \\ \rho v \\ \rho e_t \end{bmatrix} \quad F = \begin{bmatrix} \rho u \\ \rho u^2 + p - \tau_{xx} \\ \rho uv - \tau_{xy} \\ \rho u e_t + pu - u\tau_{xx} - v\tau_{xy} - k\frac{\partial T}{\partial x} \end{bmatrix}$$

$$G = \begin{bmatrix} \rho v \\ \rho vu - \tau_{yx} \\ \rho v^2 + p - \tau_{yy} \\ \rho v e_t + pv - u\tau_{yx} - v\tau_{yy} - k\frac{\partial T}{\partial y} \end{bmatrix}$$

with

$$e_t = c_v T + \frac{V^2}{2} \quad \tau_{xx} = \frac{2}{3}\mu\left(2\frac{\partial u}{\partial x} - \frac{\partial v}{\partial y}\right)$$

$$\tau_{yy} = \frac{2}{3}\mu\left(2\frac{\partial v}{\partial y} - \frac{\partial u}{\partial x}\right)$$

$$\tau_{xy} = \mu\left(\frac{\partial u}{\partial y} + \frac{\partial v}{\partial x}\right) = \tau_{yx}$$

Here, ρ is the density, u and v are the components of velocity V, p is pressure, T is temperature, τ is the viscous shear stress, and e_t is the total specific internal energy. The flow is assumed to be laminar. Air is selected as the working fluid, and is assumed to behave according to the ideal gas equation of state. The thermophysical properties such as viscosity μ, specific heat c_v and thermal conductivity k are considered to be temperature dependent. The commercial code Fluent 13.0 [17] is used for the analysis. A density-based implicit solver with a second-order upwind scheme for spatial discretization is employed. The Roe flux-difference splitting (Roe-FDS) scheme for evaluating the convective fluxes at the cell faces is used. Invoking the channel symmetry about the central axis, only half channel width is simulated.

The solver is validated by performing simulations of the experiments carried out by Sun et al. [5]. For this purpose, the computational domain (shown in Fig. 1) is identical to experimental set up of Sun et al. [5]. The walls are provided with a no-slip and isothermal boundary condition. Three different channel widths of 4, 2 and 1 mm are simulated along with two initial driven pressures of 10^5 and 10^4 Pa for a diaphragm pressure ratio of 2.352 (corresponding to an incident shock Mach number $M_s = 1.2$). The shock is generated in the larger channel and transmitted in the narrow channel, as in the case of the experiment of Sun et al. [5]. Five pressure transducers P_1, P_2, P_3, P_4, P_5 in the experimental set-up of Sun et al. [5] were set at every 50 mm distance as shown in Fig. 1. Figure 2 shows the comparison of the simulated pressure traces with the experimental pressure traces reported by Sun et al. [5]. It can be seen that the simulations are able to reproduce the experimental records with good accuracy.

An additional validation is performed with the numerical results of Parisse et al. [11]. They have simulated a geometry similar to the experimental set-up of Sun et al. [5], in

Fig. 1 Experimental setup of Sun et al. [5] showing the pressure transducer locations
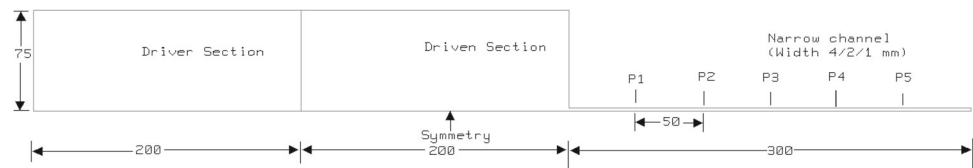
Fig. 2 Comparison of simulated pressure traces with the experimental traces recorded by Sun et al. [5]
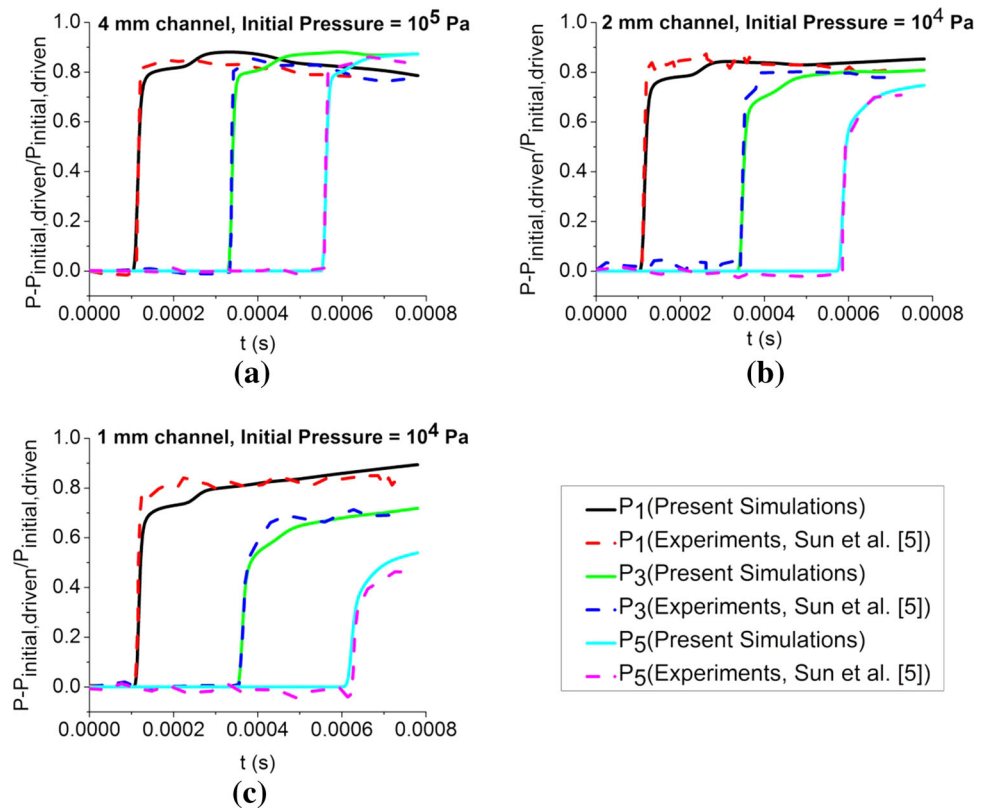
which a shock is generated in a conventional shock tube and propagated in three different channels of half heights (H) equal to 200, 100, 50 μm. The initial driven section pressure is 10^4 Pa and the driver section pressure is 2×10^6 Pa. Figure 3 shows the pressure, temperature and Mach number distributions obtained in the present numerical simulations and the numerical results of Parisse et al. [11] for $H = 100$ μm and for two time instants ($t_1 = 8.59 \times 10^{-2}$ ms and $t_2 = 10.33 \times 10^{-2}$ ms). It can be seen that the simulations are able to reproduce the numerical results of Parisse et al. [11] with good accuracy. With these two validations, the solver and the settings are used for further simulations.
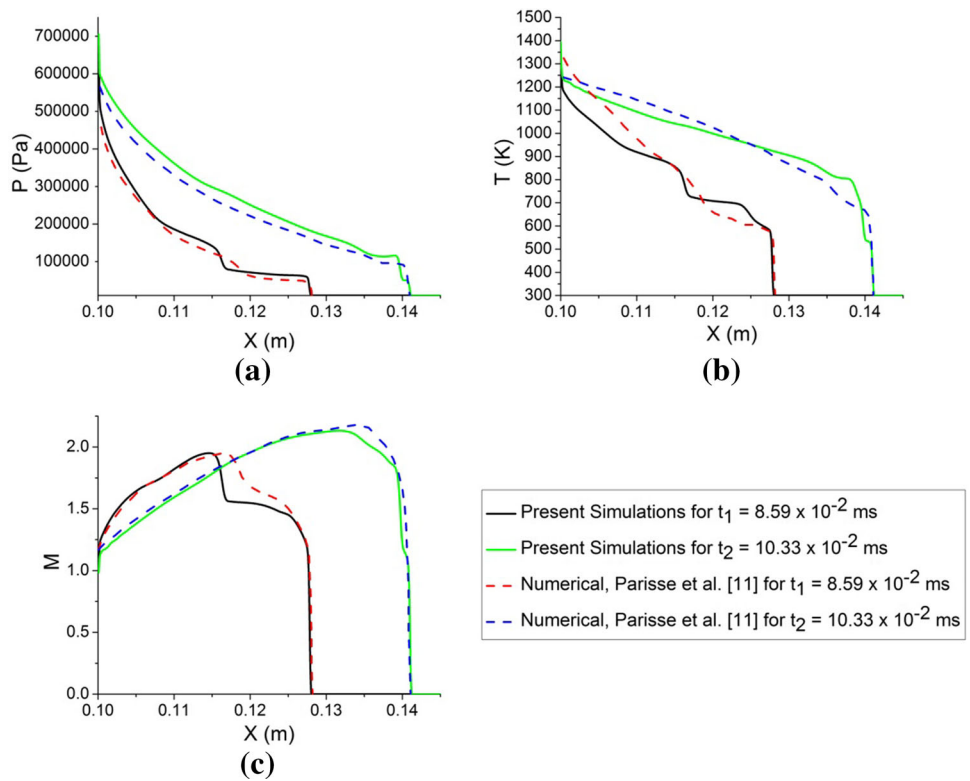
3 Parameters of the problem

The schematic of the channel used for the present simulations is shown in Fig. 4, along with the relevant nomenclature. It can be noted that the geometry of the channel has a uniform cross section, unlike having a change in the cross sections as

was the case in the experimental set-up of Sun et al. [5] and the numerical simulations of Parisse et al. [11].

A structured mesh is used with a uniform cell size along the length of the channel and a non-uniform size in the lateral direction. The cells are refined near the wall to capture the boundary layer. The grid independence of simulations is ascertained when 2,000 cells along the length and 15 cells in the lateral direction are used (Fig. 5). Similarly, the time step is determined as 5×10^{-7} s after ascertaining the time step independence.

The effects of wall heat conduction and viscosity are investigated with a parametric study. Three different channel widths, viz., 4, 2 and 1 mm are considered with three different initial pressures, viz., $10^5, 5 \times 10^4$ and 10^4 Pa in the driven section. The initial temperature everywhere is assumed to be 300 K. Additionally, three diaphragm pressure ratios of 2.352, 33.711 and 145.342 are considered. These diaphragm pressure ratios correspond to the shock Mach numbers of 1.2, 2 and 2.5, when calculated using the inviscid theory. The total length of the full domain is 1 m. For diaphragm pressure ratios 2.352, 33.711 and

Fig. 3 Comparison of pressure, temperature and Mach number distributions for $H = 100$ μm for $t_1 = 8.59 \times 10^{-2}$ and $t_2 = 10.33 \times 10^{-2}$ ms with numerical results of Parisse et al. [11]

(a)

(b)

—— Present Simulations for $t_1 = 8.59 \times 10^{-2}$ ms
—— Present Simulations for $t_2 = 10.33 \times 10^{-2}$ ms
– – – Numerical, Parisse et al. [11] for $t_1 = 8.59 \times 10^{-2}$ ms
– – – Numerical, Parisse et al. [11] for $t_2 = 10.33 \times 10^{-2}$ ms

(c)

Fig. 4 Schematic diagram of the geometry used for the present simulations
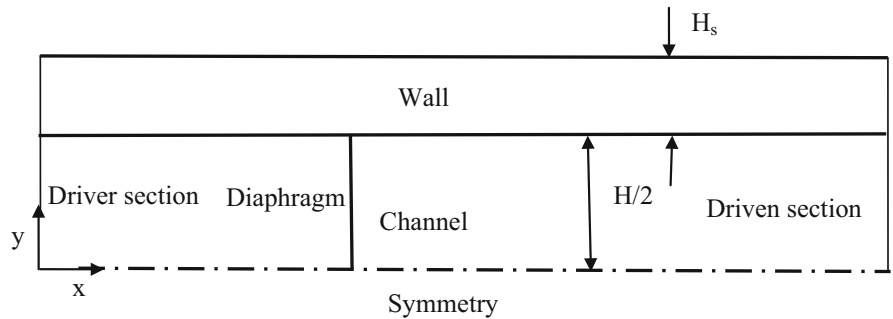
Fig. 5 Grid independence of simulations: **a** centreline pressure plot, **b** velocity profile in the post-shock region for various grids

(a)

(b)
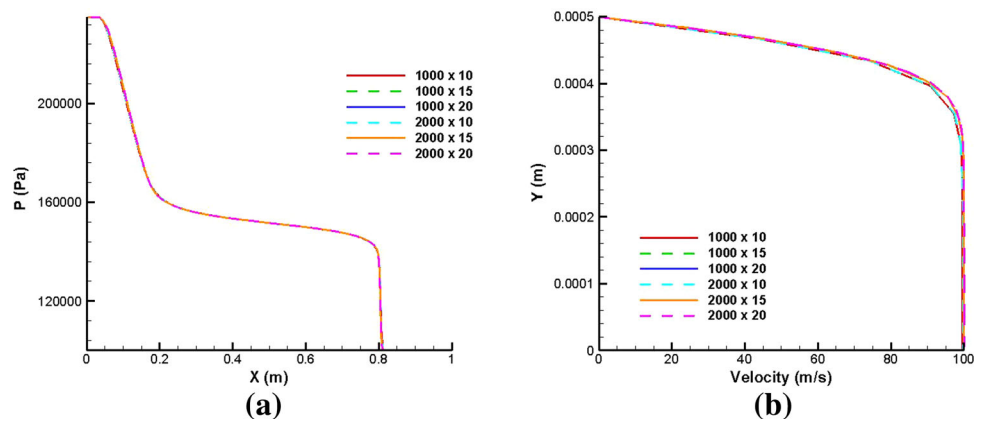
145.342, the lengths of the driver section are 0.4, 0.35 and 0.3 m, respectively, and simulation times are 1, 0.9 and 0.8 ms, respectively. These values are selected such that there is no reflection of any wave from the end walls. The Knudsen number for all simulations is less than 0.001.

Table 1 Different wall materials and the corresponding conductivity ratios, evaluated using the thermal conductivity of air at 300 K

Material	Thermal conductivity k_s (W/m/K)	Conductivity ratio $k_{sf} = k_s/k_f$
Aluminium	202.4	8,363.4
Steel	16.27	672.31
Wood	0.173	7.15

Table 2 The unit Reynolds number for different channel widths and initial driven pressure

Initial driven pressure (Pa)	Unit Reynolds number (per m)
10^5	21,840,806
5×10^4	10,920,403
10^4	2,183,328

The wall heat conduction is studied by incorporating a finite thickness solid wall bounding the flow channel (see Fig. 4). Three different materials are considered for the channel wall. These three materials result in three distinctly different thermal conductivity ratios (denoted by $k_{sf} = k_s/k_f$) between the wall material and air. Table 1 shows the conductivities of the three materials and the corresponding ratios, when evaluated using the thermal conductivity of air at 300 K. At the fluid–solid interface, a conjugate heat transfer boundary condition is employed. This condition maintains continuity of both temperature and heat flux across the interface. If the wall heat conduction is not modelled explicitly, the channel wall is assumed to be either isothermal (at 300 K) or adiabatic.

The primary dimensionless parameter of interest in the present problem is given by $\mathrm{Re}\,H/4L_s$, where H is the width of the channel and L_s is taken to be the distance travelled by the shock, following the removal of the diaphragm at $t = 0$. Here, the Reynolds number is defined as suggested by Brouillette [6], with the characteristic length scale H, the characteristic velocity being the speed of sound a in the undisturbed driven section and the characteristic physical properties corresponding to the undisturbed driven section air. Since the Reynolds number involves the channel width, a unit Reynolds number ($\mathrm{Re}_m = (\rho a/\mu)_1$) which is independent of the channel dimension is also calculated. Table 2 shows the unit Reynolds numbers for the different initial pressures. The additional dimensionless parameters due to the wall conduction are the ratio of the thermal conductivity of the wall material to that of air (k_s/k_f), and the ratio of the thickness of the solid wall to the width of the fluid channel (H_s/H). The shock attenuation is quantified in terms of the change in the shock Mach number (ΔM_s) normalized by the ideal shock Mach number (M_s) given by the inviscid theory.
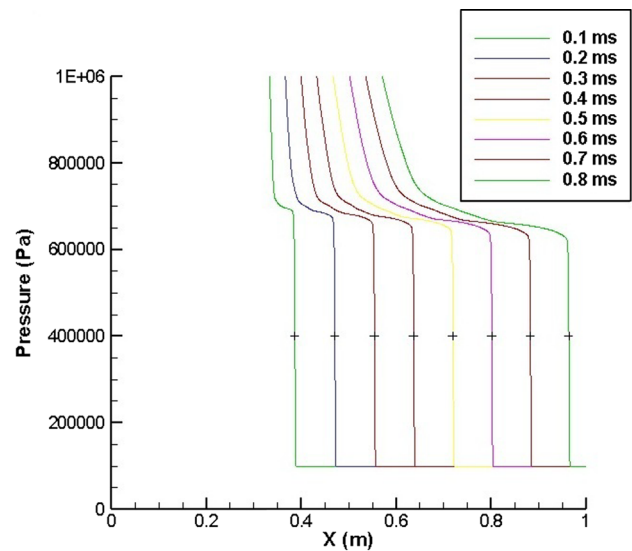
Fig. 6 Successive shock positions for the determination of the shock speed and the shock Mach number

This is denoted by $\Delta M_s/M_s$, where $\Delta M_s = M_{s,\mathrm{actual}} - M_s$. The shock Mach number ($M_{s,\mathrm{actual}}$) is determined as follows: the position of the shock is calculated at every 0.1 ms by choosing the location in the pressure distribution plots which corresponds to 50 % of the pressure jump across the shock. Once such successive positions of the shock are determined (Fig. 6), the speed of the shock and the shock Mach number are readily obtained. The shock attenuation is calculated until the shock Mach number becomes unity. Finally, it may be noted that in the 27 simulated cases, more than two hundred L_s values have been used. Furthermore, in each case these values are different. The minimum and the maximum L_s values used over this entire set of simulations are 0.084 and 0.686 m, respectively.

4 Results and discussion

4.1 Conjugate heat transfer

The effect of the parameter (H_s/H) is investigated first. For this purpose, the diaphragm pressure ratio is fixed at 2.352 and the wall material is chosen to be steel. Three different values of H_s/H are employed: 0.5, 1, 2. Figure 7 shows that the effect of H_s/H on the shock attenuation is negligible. The attenuation for different values of H_s/H can be seen to be overlapping. Similar observations are made for other wall materials and diaphragm pressure ratios, and hence H_s/H is neglected from further analysis.

To investigate the effect of wall conduction, the channel wall thickness is fixed at 1 mm since it is seen to have no effect on shock attenuation. Figure 8 shows the shock

Fig. 7 Simulation results
showing negligible effect of the
ratio of the channel wall width
to the channel width.
a Corresponds to an initial
driven section pressure of 10^5 Pa
and **b** corresponds to an initial
driven section pressure of
10^4 Pa
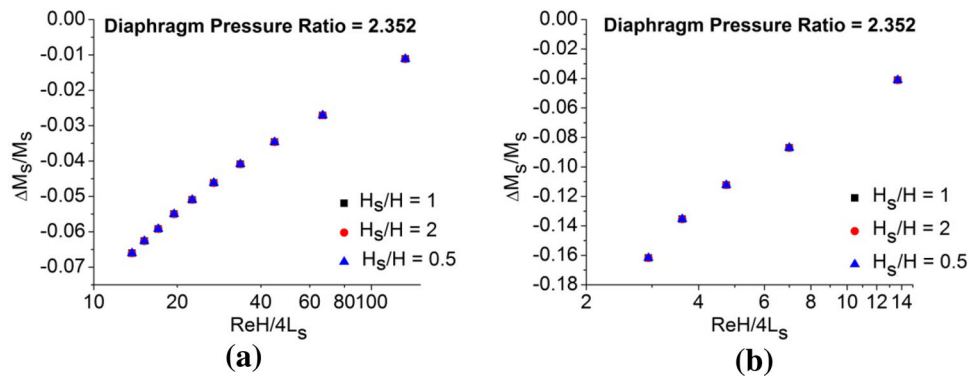
Fig. 8 Shock attenuation for
different thermal wall boundary
conditions. **a**, **c** Correspond to
an initial driven section pressure
of 10^5 Pa while **b**, **d** correspond
to an initial driven section
pressure of 10^4 Pa
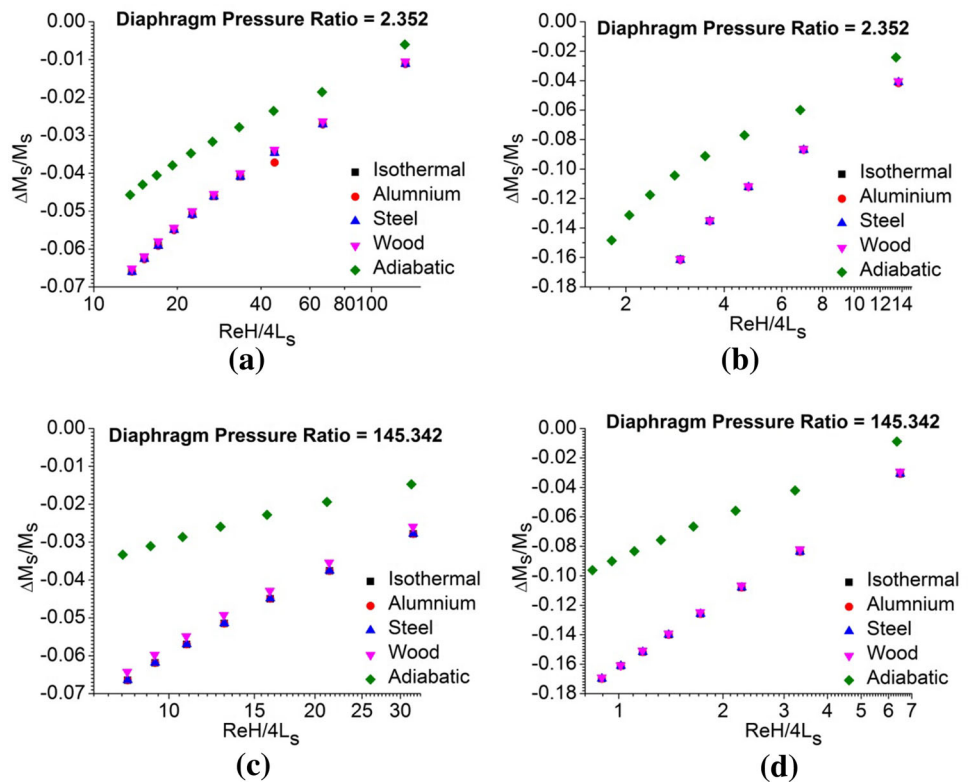
attenuation behaviour in the channel with $H = 1$ mm (representative case) for the lowest and the highest diaphragm pressure ratio (2.352 and 145.342) and for two different initial driven section pressures. In each case, the attenuation is computed for different thermal wall boundary conditions.

From each of the Fig. 8a–d, it can be seen that the shock attenuates as it travels. The attenuation increases as the shock travel increases. This behaviour is more severe for small size channels (the data for the 4 and 2 mm channels are not shown for brevity), at lower initial driven section pressures and smaller diaphragm pressure ratios. The attenuation predicted by the detailed wall conduction model is identical to that predicted by the isothermal wall model since the predicted values using both these models can be seen to be overlapping. This is even more evident at the lower value of the initial pressure in the driven section.

In view of this observation, we conclude that the wall conduction effect is adequately modelled by incorporating an isothermal wall model. On the other hand, there is significantly less attenuation of the shock if the wall is adiabatic.

To understand the role of wall heat conduction on shock attenuation, the temperature and axial velocity profiles in the region just behind the shock are plotted. Figure 9 shows these profiles for the diaphragm pressure ratio of 2.352. Figure 9a, b shows the temperature and axial velocity profiles for the initial driven section pressure of 10^5 Pa, and Fig. 9c, d shows the same two profiles for the initial driven section pressure of 10^4 Pa. The shock travel corresponds to $\text{Re}H/4L_s = 13.73$ in Fig. 9a, b, and to $\text{Re}H/4L_s = 2.935$ in Fig. 9c, d.

Fig. 9 Post-shock temperature and axial velocity profiles, showing higher values with the adiabatic wall. The predictions with the detailed wall conduction included are identical with those using an isothermal wall
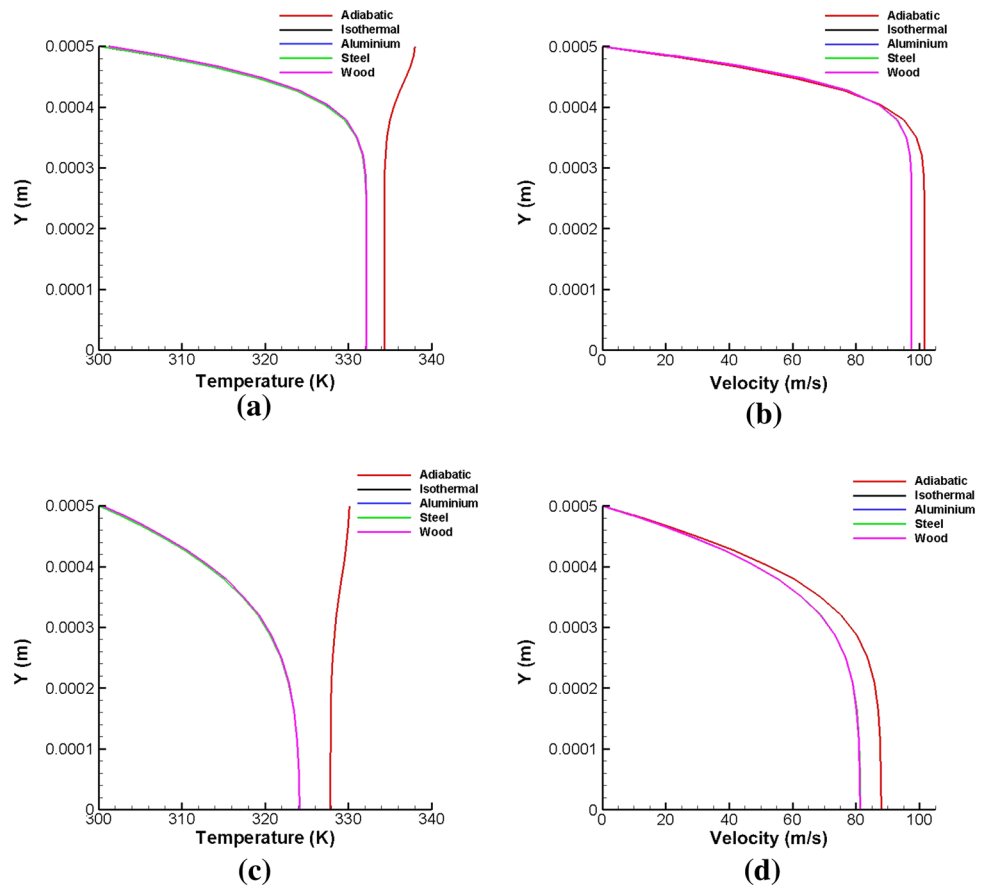
It can be seen from Fig. 9 that the adiabatic wall condition maintains higher induced velocities and post-shock temperatures, resulting in less shock attenuation. The nearly vertical behaviour of the temperature profile in Fig. 9a, c corresponds to the adiabatic wall condition. The temperature profile is normal to the channel wall due to the zero temperature gradient condition at the wall. The temperature near the wall is slightly higher than that in the bulk due mostly to viscous dissipation effects.

It may further be noted that the total time of interest of the simulations in the foregoing cases is approximately 1 ms. In such a short time, the total heat transferred due to conduction in the wall results in negligible thermal penetration depths in the walls, irrespective of the thermal conductivity and the thickness of the wall. The thermal penetration depths (d) are too small for the present CFD simulations to resolve, and hence are estimated using $d \sim \sqrt{\alpha t}$, where α is thermal diffusivity and t is time. The maximum and minimum values of the penetration depths are estimated to be approximately 0.3 mm and 10 μm respectively, which are much smaller than the channel wall thickness. These results are in accordance with the explanations provided by Mirels [3] and Parisse et al. [11], where it is pointed out that the thermal conductivity of the solid wall is much larger than that of the gas, resulting in an efficient distribution of

the heat transferred in the wall, which maintains the wall essentially isothermal. On the other hand, if the wall conduction is completely prevented (adiabatic condition), the higher energy content and induced velocity in the post-shock region result in less shock attenuation, as shown in Fig. 9. Hence, the shock attenuation is dependent on wall heat conduction but is essentially independent of the thermal conductivity of the wall material. In an analogous manner, it can be noted that the thickness of the channel wall is immaterial (as seen in Fig. 7) as long as it is much larger than the thermal penetration depths achieved during the times of interest.

4.2 Effect of diaphragm pressure ratio

When the initial Mach number is increased by increasing the diaphragm pressure ratio while keeping the initial pressure in the driven section constant, the attenuation is seen to be less for a given value of $\mathrm{Re}\,H/4L_s$ (see Fig. 8a, c or Fig. 8b, d). Table 3 shows the attenuation data for these three cases. In such cases, the Reynolds number is identical, since the initial driven section pressure is the same. For a channel of fixed H, this implies that the shock travel L_s is the same for a given value of $\mathrm{Re}\,H/4L_s$. Higher initial Mach numbers are associated with higher induced velocities. Additionally, the

Table 3 Contribution of wall heat conduction and viscous effect to shock attenuation with increasing diaphragm pressure ratios

Diaphragm pressure ratio	Initial driven section pressure (Pa)	$\mathrm{Re}H/4L_s$	$\Delta M_s/M_s$	Contribution due to viscous effects (%)	Contribution wall heat transfer (%)
2.352	10^5	13.73	−0.066	69	31
33.711	10^5	13.73	−0.056	56	44
145.342	10^5	13.73	−0.049	51	49
2.352	10^4	2.935	−0.161	64	36
33.711	10^4	2.935	−0.114	59	41
145.342	10^4	2.935	−0.090	51	49

Fig. 10 Post-shock temperature and velocity profiles showing thinner boundary layers with increasing diaphragm pressure ratios. **a**, **b** Correspond to the initial driven section pressure of 10^5 Pa, $\mathrm{Re}H/4L_s = 13.73$ and **c**, **d** correspond to the initial driven section pressure of 10^4 Pa, $\mathrm{Re}H/4L_s = 2.935$
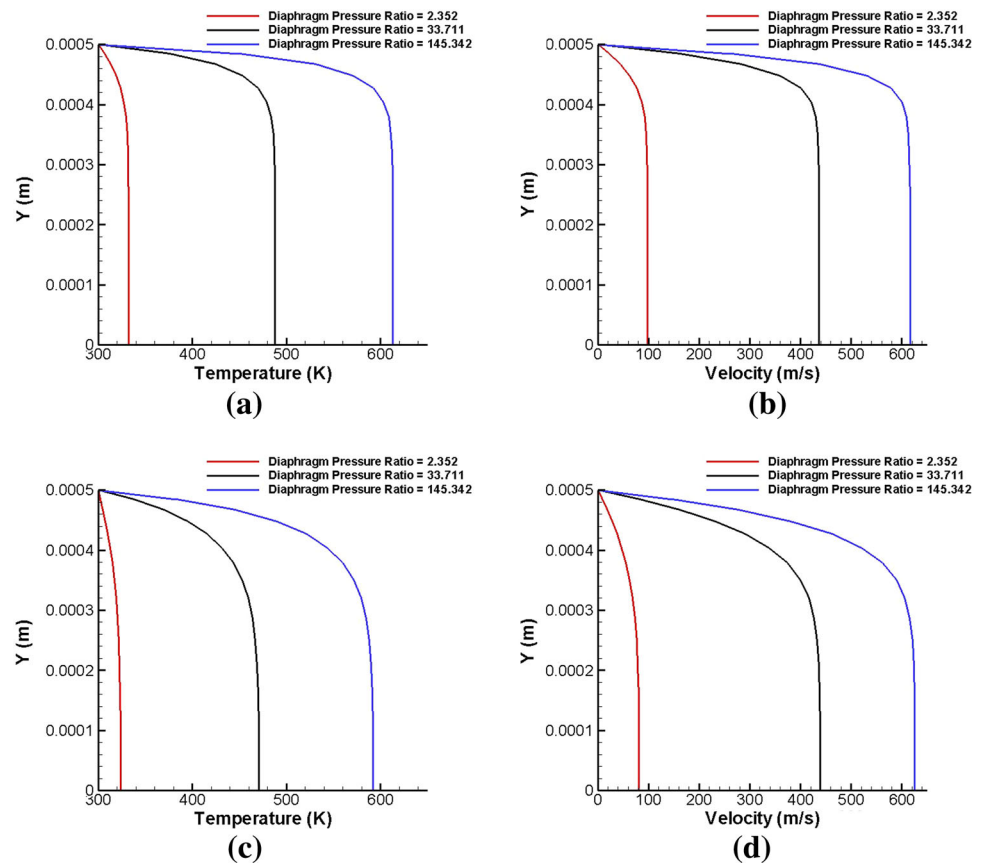
relatively low kinematic viscosity in the post-shock region coupled with a comparatively shorter time taken by the shock for a given travel distance L_s results in thinner boundary layers in the post-shock region (see Fig. 10). This effect is even more pronounced at lower initial driven section pressures (Fig. 10c, d). Therefore, the viscous effects are reduced at higher diaphragm pressure ratios, resulting in less attenuation.

At this point, the relative contributions of the wall heat conduction and the viscous effects on shock attenuation are discussed. It can be seen from Fig. 8 that the shock attenuation has contributions from both the viscous effects and wall heat transfer. For a given value of $\mathrm{Re}H/4L_s$ in any of the four

plots presented in Fig. 8, the data point corresponding to the "Adiabatic" wall condition provides the contribution to shock attenuation only due to viscous effects. The additional contribution due to wall heat transfer is provided by the data point corresponding to the "Isothermal" wall condition. For given values of $\mathrm{Re}H/4L_s$ and initial pressure, the contribution of wall heat conduction to shock attenuation increases at higher diaphragm ratios. This is evident from Table 3. With identical $\mathrm{Re}H/4L_s$ and initial pressure values, the shock takes less time to travel a certain distance L_s at higher diaphragm ratios. This implies thinner boundary layers in the post-shock region and, consequently, increased contribution of wall heat transfer.

Table 4 Contribution of wall heat conduction and viscous effects to shock attenuation with decreasing initial pressure in the driven section

Diaphragm pressure ratio	Initial driven section pressure (Pa)	$\mathrm{Re}H/4L_s$	$(\Delta M_s/M_s)$	Contribution due to viscous effects (%)	Contribution due to wall heat transfer (%)
2.352	10^5	13.66	−0.066	70	30
2.352	10^4	13.66	−0.041	58	42
33.711	10^5	9.17	−0.071	55	45
33.711	10^4	9.17	−0.031	38	62
145.342	10^5	8.22	−0.067	50	50
145.342	10^4	8.22	−0.022	11	89
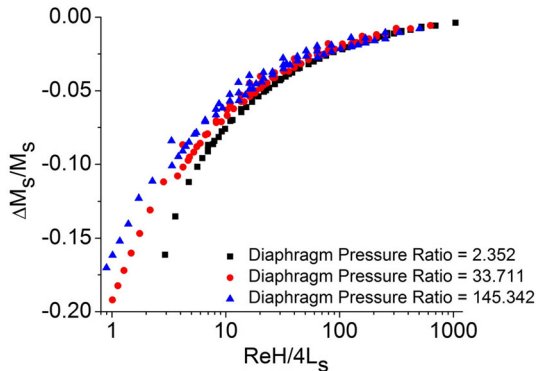
Fig. 11 Shock attenuation data from the entire parametric study consisting of 27 cases

4.3 Effect of initial pressure in the driven section

For the same value of $\mathrm{Re}H/4L_s$, as the initial pressure is reduced keeping the diaphragm ratio constant, the attenuation is seen to be less (see Fig. 8a, b or Fig. 8c, d). Table 4 shows the attenuation data for these cases. As the initial pressure in the driven section is decreased while maintaining the same diaphragm ratio, the Reynolds number is reduced through the reduction of density in the driven section. Therefore, to achieve a certain value of $\mathrm{Re}H/4L_s$, the shock travel is less. Additionally, since the shock speed is identical even as the initial driven section pressure decreases, the time taken for the shock travel is less. This implies thinner boundary layers in the post-shock region and hence less attenuation.

For given values of $\mathrm{Re}H/4L_s$ and diaphragm pressure ratio, if the initial pressure in the driven section is reduced, the effect of wall heat conduction on shock attenuation relative to that of viscosity is higher. This is evident from Table 4. With reduction in the initial driven section pressure, the shock travel L_s is smaller to achieve a certain value of $\mathrm{Re}H/4L_s$. Since the diaphragm ratio is the same, the shock speed is the same, resulting in shorter time required to achieve the smaller shock travel. The reduced time corresponds to a higher contribution of wall heat transfer as before.
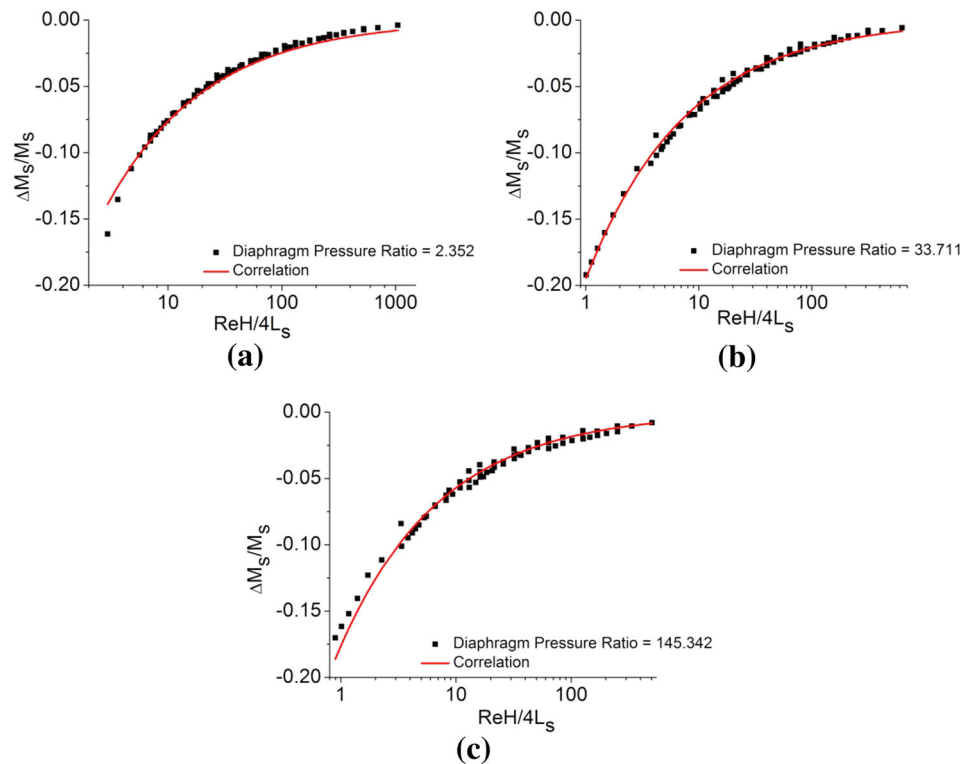
4.4 Correlations

The attenuation data for the other channel heights (4 and 2 mm) are qualitatively similar to those for the channel height for which results are presented (1 mm) in the foregoing sections. The entire set of data, generated from the parametric study consisting of three channel widths, three diaphragm pressure ratios p_4/p_1 and three initial driven section pressures p_1 (see Sect. 3 for their values), is presented in Fig. 11.

A correlation given by

$$\frac{\Delta M_s}{M_s} = -0.25 \left(\frac{\mathrm{Re}H}{4L_s}\right)^{-0.49} \left(\frac{p_4}{p_1}\right)^{-0.07} \tag{2}$$

is fitted to the entire data set, with 82 % of data within ±15 % of the values predicted using the correlation. The correlation can be considered to be applicable for the following ranges of the two independent dimensionless parameters: $0.9 < \mathrm{Re}H/4L_s < 1{,}045$ and $2.352 < p_4/p_1 < 145.342$. A comparison between the attenuation predicted using the proposed correlation and the data from the numerical simulations for the three different diaphragm pressure ratios is shown in Fig. 12. As long as the operating conditions pertaining to a shock-channel geometry (as shown in Fig. 4, including micron-size channels) result in dimensionless parameters that are within the range of validity of the proposed correlation, and if the continuum assumption can be considered to be applicable, the correlation can be used to estimate the attenuation. It can be noted from the correlation that the influence of the diaphragm pressure ratio on shock attenuation is small. This is consistent with the ideal inviscid theory, where the shock pressure ratio is a weak function of the diaphragm pressure ratio. In the present situation of a viscous shock tube, the initial shock pressure ratio (and hence the initial shock speed) is what is determined by the diaphragm pressure ratio. Since the initial shock speed is weakly influenced by the diaphragm pressure ratio, the subsequent attenuation follows a similar trend. The parameter $\mathrm{Re}H/4L_s$ signifies a combination of viscous forces and the dimensionless shock travel, and is expected to have a larger significance on shock attenuation. The correlation, generated from

Fig. 12 Comparison between the attenuation predicted using the proposed correlation and the attenuation data from the numerical simulations

Table 5 Correlations generated using the data from the parametric study

Range for $\mathrm{Re}H/4L_\mathrm{s}$	Correlation	Data within ± 15 % of the values predicted using the correlation (%)
$\mathrm{Re}H/4L_\mathrm{s} > 100$	$\frac{\Delta M_\mathrm{s}}{M_\mathrm{s}} = -0.42 \left(\frac{\mathrm{Re}H}{4L_\mathrm{s}}\right)^{-0.64} \left(\frac{\mathrm{p}_4}{\mathrm{p}_1}\right)^{-0.01}$	86
$10 < \mathrm{Re}H/4L_\mathrm{s} < 100$	$\frac{\Delta M_\mathrm{s}}{M_\mathrm{s}} = -0.25 \left(\frac{\mathrm{Re}H}{4L_\mathrm{s}}\right)^{-0.51} \left(\frac{\mathrm{p}_4}{\mathrm{p}_1}\right)^{-0.05}$	93
$\mathrm{Re}H/4L_\mathrm{s} < 10$	$\frac{\Delta M_\mathrm{s}}{M_\mathrm{s}} = -0.25 \left(\frac{\mathrm{Re}H}{4L_\mathrm{s}}\right)^{-0.47} \left(\frac{\mathrm{p}_4}{\mathrm{p}_1}\right)^{-0.08}$	100

the simulations data, does represent these physical aspects appropriately.

The accuracy of the correlation is improved by dividing the data into three sets, each corresponding to a range of the parameter $\mathrm{Re}H/4L_\mathrm{s}$ ($\mathrm{Re}H/4L_\mathrm{s} > 100$, $10 < \mathrm{Re}H/4L_\mathrm{s} < 100$ and $\mathrm{Re}H/4L_\mathrm{s} < 10$). The correlations for the three ranges of $\mathrm{Re}H/4L_\mathrm{s}$ are given in Table 5.

5 Conclusion

The effects of diffusive transport phenomena due to viscosity and wall heat conduction on shock propagation and attenuation in narrow channels are numerically investigated in this work. The present investigation indicates that while the effect of wall heat conduction on shock attenuation is significant and cannot be neglected, the isothermal boundary condition at the channel wall is sufficient to model it. It is further concluded that the conductivity and thickness of the wall material have negligible effect on shock attenuation. This is due to the fact that the thermal penetration depths in the wall for different wall conductivity and thickness values, while non-zero, are negligibly small for the typical times of interest (≈ 1 ms). The shock attenuation behaviour and the relative contributions of viscous effects and wall heat transfer on shock attenuation are explained on the basis of boundary layer formation in the post-shock region. The parametric study performed using different values of diaphragm pressure ratios and initial pressures in the driven section indicates that the effect of viscosity is more dominant in the shock attenuation process.

References

1. Duff, R.E.: Shock-tube performance at low initial pressure. Phys. Fluids **2**(2), 207–216 (1959)
2. Roshko, A.: On flow duration in low-pressure shock tubes. Phys. Fluids **3**(6), 835–842 (1960)
3. Mirels, H.: Test time in low-pressure shock tubes. Phys. Fluids **6**(9), 1201–1214 (1963)
4. Mirels, H.: Correlation formulas for laminar shock tube boundary layer. Phys. Fluids **9**(7), 1265–1272 (1966)
5. Sun, M., Ogawa, T., Takayama, K.: Shock propagation in narrow channels. In: Proceedings of the 23rd ISSW, Fort Worth, Texas, USA, 22–27 July, pp. 1320–1326 (2001)
6. Brouillette, M.: Shock waves at microscales. Shock Waves **13**, 3–12 (2003)
7. Mirshekari, G., Brouillette, M.: One-dimensional model for microscale shock tube flow. Shock Waves **19**, 25–38 (2009)
8. Ngomo, D., Chaudhuri, A., Chinnayya, A., Hadjadj, A.: Numerical study of shock propagation and attenuation in narrow tubes including friction and heat losses. Comput. Fluids **39**, 1711–1721 (2010)
9. Zeitoun, D.E., Burtschell, Y.: Navier–Stokes computations in micro shock tubes. Shock Waves **15**, 241–246 (2006)
10. Zeitoun, D.E., Burtschell, Y., Graur, I.A., Ivanov, M.S., Kudryavtsev, A.N., Bondar, Y.A.: Numerical simulation of shock wave propagation in microchannels using continuum and kinetic approaches. Shock Waves **19**, 307–316 (2009)
11. Parisse, J.D., Giordano, J., Perrier, P., Burtschell, Y., Graur, I.A.: Numerical investigation of micro shock waves generation. Microfluid Nanofluid **6**, 699–709 (2009)
12. Shoev, G.V., Bondar, Y.A., Khotyanovsky, D.V., Kudryavtsev, A.N., Mirshekari, G., Brouillette, M., Ivanov, M.S.: Numerical study of the shock wave propagation in a micron-scale contracting channel. In: Proceedings of the 27th International Symposium On Rarefied Gas Dynamics, Pacific Grove, California, USA, 10–15 July (2010)
13. Shoev, G.V., Bondar, Ye A., Khotyanovsky, D.V., Kudryavtsev, A.N., Maruta, K., Ivanov, M.S.: Numerical study of the shock wave entry and propagation in a microchannel. Thermophys. Aeromech. **19**(1), 17–32 (2012)
14. Austin, J.M., Bodony, D.J.: Wave propagation in gaseous small-scale channel flows. Shock Waves **21**, 547–557 (2011)
15. Arun, K.R., Kim, H.D.: Computational study of the unsteady flow characteristics of a micro shock tube. J. Mech. Sci. Technol. **27**(2), 451–459 (2013)
16. Mirshekari, G., Brouillette, M., Giordano, J., Hébert, C., Parisse, J.D., Perrier, P.: Shock waves in microchannels. J. Fluid Mech. **724**, 259–283 (2013)
17. Ansys Fluent 13.0 User's Guide (2010)